Environmental Nanotechnology, Monitoring & Management 23 (2025) 101083

Contents lists available at ScienceDirect

Environmental Nanotechnology, Monitoring & Management

journal homepage: www.elsevier.com/locate/enmm

Antimony retention and transformation: a novel approach using microfluidics and hydrogel, biocomposite nanomagnetite aggregates

Evgenia-Maria Papaslioti [a,b,*], Hervé Tabuteau [c], Julien Farasin [c], Delphine Vantelon [d], Valerie Magnin [a], Laurent Charlet [a]

[a] Univ. Grenoble-Alpes, Univ. Savoie Mont Blanc, CNRS, IRD, Univ. Gustave Eiffel, ISTerre, 38000 Grenoble, France
[b] Department of Earth Sciences & Research Center on Natural Resources, Health and the Environment, University of Huelva, Campus "El Carmen", E-21071 Huelva, Spain
[c] Univ Rennes, CNRS, IPR (Institut de Physique de Rennes) -UMR 6251, F-35000 Rennes, France
[d] Synchrotron SOLEIL, L'Orme des Merisiers, Départementale 128, 91190 Saint-Aubin, France

ARTICLE INFO

Keywords:
Antimony
Nanomagnetite
PEGDA/chitosan bio-nanocomposites
Microfluidics
Synchrotron X-ray spectroscopy
Remediation technique

ABSTRACT

Antimony (Sb) is a redox sensitive metalloid increasingly recognized as an emerging contaminant of global concern due to its toxicity and widespread occurrence in natural and anthropogenically impacted water systems. It is commonly found in both drinking and wastewater, where it poses potential risks to human health. Magnetite nanoparticles, known as active retention agents for redox-sensitive contaminants, are combined here with polymeric matrices to ease their application in water treatment systems and to enhance their stability, dispersibility, and sorption efficiency. In this study, we assess Sb retention using hydrogel-nanomagnetite aggregates, with and without chitosan coating, under flow-through microfluidic conditions that mimic natural and engineered aquatic environments. Advanced synchrotron-based μ-XRF mapping and μ-XANES spectroscopy were employed for the first time to such integrated system to simultaneously resolve the spatial distribution and oxidation state of sorbed Sb. Antimonate immobilization followed two distinct, input concentration-dependent pathways: (i) reduction to Sb(III), forming stable inner-sphere Fe–O–Sb complexes, or (ii) adsorption via electrostatic and complexation mechanisms. At low Sb(V) concentrations reduction is favored in chitosan-free aggregates, enabling homogeneous Sb(III) diffusion through the media. At higher concentrations, and particularly in chitosan-coated systems, Sb(V) is immobilized predominantly via adsorption, accumulating on the rim of the aggregates. Chitosan enhances Sb(V) sorption by providing positively charged functional groups and, along with pH and Sb input concentration, controls Sb sorption processes. These findings deepen the understanding of Sb retention mechanisms through redox and sorption interactions in polymer-supported magnetite systems, as revealed using microfluidics technology, and provide a new foundation for the development of advanced water treatment technologies with international relevance for mitigating redox-sensitive contaminants.

1. Introduction

Antimony is a redox sensitive, toxic, and anthropo-geo-genic metalloid, ubiquitously present in the environment. It mainly occurs in nature as trivalent solid Sb(III) species, such as stibnite (Sb_2S_3) and valentinite (Sb_2O_3), both being commonly present in coal and petroleum (Filella et al., 2002). In the aquatic environment aqueous antimony is present in the form of pentavalent Sb(V) species as the result of Sb bearing mineral weathering, soil runoff and anthropogenic activities (Filella et al., 2002). Antimony and its compounds are listed as priority pollutants by the U.S. Environmental Protection Agency (USEPA) (United States Environmental Protection Agency, 1979) and the European Union (Council of the European Communities, 1976), due to their potential for bioaccumulation and adverse effects on human health. The maximum admissible Sb concentration in drinking water has been set up at 20 μg/L by the World Health Organization (WHO), and at 5 μg L^{-1} by the European Union (Council of the European Union, 1998). Human exposure routes to Sb include breathing, eating, drinking, and skin

* Corresponding author at: Department of Earth Sciences & Research Center on Natural Resources, Health and the Environment, University of Huelva, Campus "El Carmen", E-21071 Huelva, Spain.
E-mail address: evgeniamaria.papaslioti@dct.uhu.es (E.-M. Papaslioti).

https://doi.org/10.1016/j.enmm.2025.101083
Received 6 February 2025; Received in revised form 5 May 2025; Accepted 4 June 2025
Available online 4 June 2025

contact. Excess intake may cause cardiotoxicity, pulmonary toxicity, and genotoxicity cancer health problems (Wilson et al., 2010; Boreiko and Rossman, 2020). The global use of Sb in a range of industrial applications has increased, from brake pads and storage battery lead-alloy to ammunition and flame retardant, generating great quantities of Sb-bearing wastes (Fu et al., 2023; Zhang et al., 2022). These activities contribute to Sb continuous migration into aquatic environments, and as such, environmental concern has recently gained a worldwide recognition that focuses on its toxicity and bioavailability (Fu et al., 2023; Zhang et al., 2022). Therefore, Sb contamination of drinking and wastewaters, and consequently, the related novel decontamination techniques have attracted worldwide attention, trying to overcome the scarcity of available adsorbents to comply with regulatory, very low concentration limit, particularly for the dominant Sb(V) form.

Antimony speciation in biological and environmental systems is of primary significance, since Sb geochemical behavior and toxicity depend on Sb redox state, with pentavalent Sb(V) species being more soluble and abundant, though less toxic, than trivalent Sb(III) species (Filella et al., 2002; Boreiko and Rossman, 2020; Filella et al., 2009). This distinction plays a crucial role in assessing the environmental and health risks of antimony contamination. While Sb(V) species are mentioned as part of the broader antimony biotransformation pathway, Sb(III) is generally considered the more toxic form due to its ability to interfere with cellular processes and cause tissue damage at lower thresholds (Boreiko and Rossman, 2020). In aqueous environments, Sb (III) typically exists as the neutral species $Sb(OH)_3$, which tends to be more mobile and readily taken up by organisms compared to the anionic forms of Sb(V), such as $Sb(OH)_6^-$ (Zhang et al., 2022). As such, Sb(III) adsorbed to iron oxides is less mobile than Sb(V), outcompeting and mobilizing it for sorption sites over a wide pH range (i.e. 3–10) (Guo et al., 2014; Qi and Pichler, 2016). Antimony shares many physicochemical similarities with As, and thus, they have been reported to behave similarly during redox, geochemical processes (Council of the European Union, 1998; Casiot et al., 2007). However, Sb is much more understudied compared to As, despite its greater worldwide production (Wilson et al., 2010), dominated by mining in China and a few other places (Fu et al., 2023). As such, the presented research focuses on the geochemical sorption processes of Sb during a promising remediation method targeting Sb contaminated waters, although potentially, applicable to various inorganic contaminants, as well.

Iron (oxyhydr)oxides have the greatest Sb adsorption capacity among solid phases (Missana et al., 2009), and their ability to retain metals on their surface is an important factor of Sb immobilization. Controlled experimental systems mimicking in-situ conditions are necessary to study the geochemical processes controlling Fe transformation and subsequent retention or release of such contaminants. Although the immobilization of contaminants by various Fe(III) (hydr) oxides (e.g. ferrihydrite, hematite) has been widely studied, magnetite (a mixed Fe(II) and Fe(III) oxide) is far less documented, though able to induce reductive sorption of a variety of redox active contaminants (e.g. Missana et al., 2009; Verbinnen et al., 2013). In addition, while contaminants retention by Fe minerals in reactive transport systems, in the presence of microorganisms is well established (Pallud et al., 2010), such studies under abiotic conditions are limited. Antimony has been, reported to be efficiently immobilized by magnetite (Verbinnen et al., 2013; Kirsch et al., 2008; Mittal et al., 2013). For instance, time and pH dependence of Sb reduction reaction by magnetite, and the nature of the resulting surface complexes, were investigated using XAS, showing Sb (V) to be reduced to Sb(III) at the surface of magnetite nanoparticles in strict anoxic conditions (Kirsch et al., 2008). The reduced Sb(III) forms a highly symmetrical and stable tridentate sorption complex at the position otherwise occupied by tetrahedral Fe(III) (Kirsch et al., 2008).

Polymeric coatings can be used to stabilize iron oxide/hydroxides with respect to aggregation, as does organic matter in soils, maximizing their adsorption capacity (Wu et al., 2008; He et al., 2016). This kind of composite materials (e.g., magnetic nanoparticles embedded in a polymer matrix) facilitates also, a more efficient separation of the iron oxy(hydr)oxides from the treated water due to their large size (e.g., by filtration), enabling the particles to sediment by gravity, or to be removed by a magnetic field (He et al., 2016; Wang et al., 2009; Zou et al., 2011). In such bio-nanocomposite porous aggregate, the sorption processes and the surface reactions at the mineral water-interface depend on the water flow and on the diffusive vs. advective transport of the contaminant in the pore space (Maher and Mayer, 2019; Wielinski et al., 2022). Therefore, spatially resolved information on the distribution and speciation of the contaminants and its dependence on hydrodynamics is required at a microscale format before upscaling the system to field applications. Microfluidics technology is the ideal tool for such preliminary studies since it allows to unravel the coupling between water-water and water–solid reactions at the pore scale, despite the model aggregates proposed do not represent the whole complexity of natural systems (Wielinski et al., 2022).

Recent years have seen a growing shift toward the use of green nanotechnology and multifunctional composite materials for addressing environmental and societal challenges, particularly in the areas of pollution remediation, energy production, and health-related applications (Mubarak et al., 2015; Long et al., 2020). Green nanotechnology seeks to minimize the environmental footprint of material synthesis while maximizing performance through the use of renewable, biocompatible, or low-toxicity components. This paradigm has led to the design of responsive nanocomposites—often based on metal oxides, bio-based polymers, or hybrid systems—that are applicable in clean water production, medical diagnostics, energy storage, and environmental sensing (Long et al., 2020). In the field of environmental remediation, iron- and carbon-based nanomaterials embedded in biodegradable polymer matrices have been successfully employed to enhance contaminant sorption, facilitate recovery, and reduce secondary pollution. These systems have shown promise not only for metals like arsenic, lead, or chromium, but also for less studied metalloids such as antimony (Bai et al., 2022). For instance, cellulose-supported or starch-bridged iron composites offer high adsorption efficiency under realistic pH and flow conditions, while leveraging renewable resources to reduce environmental cost (Bai et al., 2022). More broadly, the functional versatility of these green composites—ranging from water treatment to biomedical and energy-related uses—demonstrates their potential to contribute to sustainable technologies that address both environmental degradation and human health (Mubarak et al., 2015; Long et al., 2020).

In the present work, we investigate Sb retention, using bio-nanocomposite aggregates—comprising Polyethylene Glycol Diacrylate (PEGDA), chitosan, and magnetite nanoparticles —embedded within a microfluidic chip to simulate natural systems at the microscale. This setup enables the detailed observation of time-dependent Sb sorption and redox processes under controlled flow-through conditions, providing key insights before upscaling to more complex water treatment systems. By coupling microfluidics with high-resolution synchrotron-based X-ray spectroscopy (μ-XANES and μ-XRF), we resolve both the spatial distribution and oxidation state of sorbed Sb within the porous aggregates. Building on prior findings of Sb adsorption and reduction on magnetite (Verbinnen et al., 2013; Kirsch et al., 2008), we aim to (i) quantify the time resolved removal kinetics of aqueous Sb by cylindrical nanomagnetite hydrogel composite aggregates, (ii) describe the parameters (e.g. pH, redox conditions, Sb concentration) that control sorption processes, and (iii) characterize the nature of the resulting surface complexes. This approach provides a mechanistic understanding of the coupled redox and sorption pathways that govern Sb immobilization—knowledge critical for designing efficient remediation systems. To our knowledge, this is the first study to apply such an integrated system to investigate Sb behavior, offering a novel perspective on the use of polymer-supported magnetite for contaminant removal. The insights gained here are directly relevant for the advancement of globally applicable water treatment strategies aimed at redox-sensitive elements, addressing urgent international needs for safe and sustainable water

management.

2. Materials and methods

2.1. Synthesis and characterization of nanomagnetite

Magnetite nanoparticles were synthesized under anoxic conditions following the protocol of Jolivet et al. (1992). A solution containing 0.4 M $FeCl_2{\cdot}4H_2O$ (Sigma-Aldrich) and 0.8 M $FeCl_3{\cdot}6H_2O$ (Merck), resulting in a final iron concentration of 0.55 M with an [Fe(II)]/[Fe(III)] ratio of 0.5, was prepared in 50 mL of deoxygenated water. Subsequently, 60 mL of 6 M NH_3 (Sigma-Aldrich) was slowly added to the iron solution while maintaining anoxic conditions. The solution turned black immediately upon mixing, indicating the formation of magnetite, and was left for 24 h on a rotary shaker. The magnetic nanoparticles were then separated using a strong magnet, and the supernatant was filtered through a 0.22 μm MF-Millipore membrane. The precipitate was rinsed four times with deoxygenated Milli-Q water and two times with 0.1 mM NaCl solution, which was also used as the storage medium. The final suspension had a magnetite concentration of 6.96 $g{\cdot}L^{-1}$, equivalent to 0.006 mM of reactive surface sites, and a near-neutral pH of ~7. The synthesis and storage were carried out entirely under anoxic conditions using either nitrogen sparging or a glovebox system.

The synthesized magnetite was characterized via X-ray diffraction (XRD), Mössbauer spectrometry, and transmission electron microscopy (TEM), that showed an average crystallite size of 15 nm, and a large distribution of particles ranging from 5 to 50 nm, aggregated in large clusters (Poulain et al., 2022). The specific surface area (SSA) was calculated equal to 70 m^2/g from the Brunauer – Emmett – Teller adsorption method (BET), at the P/P_0 range of 0.052 – 0.307. The detailed methodology and the characterization of the material can be found at Poulain et al. (2022).

2.2. Preparation of hydrogel – Nanomagnetite composite suspension

For the chitosan-coated nanomagnetite composite, the magnetite suspension was dispersed in de-oxygenated 2 % chitosan (CS) solution (high molecular weight chitosan from Sigma-Aldrich diluted with 1 % v/v acetic acid solution) at a volume ratio of 0.5:1 (CS:NPs). The reaction mixture was then sonicated for 15 min at 37 Hz to ensure adequate coating and to avoid any future agglomeration tendency. Chitosan is the second abundant polysaccharide present in nature, and was selected for its non-toxic, biocompatible and slower biodegradable characteristics (Wu et al., 2008). The large chitosan molecule is slightly positively charged at pH 7 (pK_a = 6.2 (de Alvarenga, 2011), and adsorbs on magnetite nanoparticles, which have near equal positive and negative surface charge around pH 7 (pHpzc = 6.5 (Milonjić et al., 1983; Kosmulski, 2004), through specific or electrostatic interactions.

The hydrogel matrix was prepared using a fully deoxygenated aqueous solution containing 50 wt% PEG-diacrylate (average Mn 700, Sigma-Aldrich) and 2 wt% of the photoinitiator 2-hydroxy-2-methylpropiophenone (97 %, Sigma-Aldrich). PEGDA was chosen to form the network of the hydrogel matrix due to its small molecular weight that does not allow it to swell with water. The PEGDA solution was then, mixed with the chitosan-coated magnetite suspension at a volume ratio of 1:1, and sonicated for 20 min at 37 Hz.

A second variant of the composite was synthesized using the same PEGDA solution mixed with pure nanomagnetite suspension, i.e., without chitosan coating, at a volume ratio of PEGDA:NPs = 1:1, following the same process. The resulted hydrogel-NPs suspensions were stored, protected against the UV light and oxidation, until further use.

2.3. Fabrication of bio-nanocomposites and microfluidic flow-through experiments

The flow-through sorption experiments were conducted in microfluidic channels fabricated from NOA 81 (Norland Optical Adhesive), a UV-curable optical glue that allows direct X-ray measurements and is impermeable to gases (Weinhausen and Köster, 2013; Neckel et al., 2021). The straight NOA channels were 7.7 mm long, 1 mm wide, and 120 μm thick, and were sealed with standard microscope glass slides (Fig. 1**A**). To fabricate the bio-nanocomposites inside the channels, the previously described nanocomposite suspensions were injected into the device through air tight connector and tubing (Fig. 1**A**). Then, suspensions were exposed to UV light through an opaque chrome photomask containing a 400 μm-diameter transparent circular opening. UV curing (wavelength ~ 365 nm) was applied for approximately 60 s to form a hydrogel-based cylindrical aggregate (i.e. pillar) at the center of the channel (Fig. 1**B**). The remaining, uncured suspension was removed by flushing deoxygenated milli-Q water through the channel. Numerous, separate microfluidic channels were prepared for each type of composite material (with and without chitosan), and were stored in UV light-protected, anoxic conditions until their use for the experiments.

For the flow-through tests, synthetic Sb(V) solutions, with concentration ranging from 2 to 15 mM, were continuously supplied at a flow rate of 20 μL min^{-1} for 24 h, using a syringe pump (SPLG100, WPI) (Fig. 1**B**). Samples were collected regularly at the outlet for the entire duration of the experiments (Fig. 1**B**). Both the fabrication of the pillars and the experiments were conducted under anoxic conditions.

2.4. Preparation of contaminant solutions and chemical analysis

Stock Sb(V) solutions of different concentrations were prepared using deoxygenated Milli-Q water, in a 1.5 mM NaCl ionic background to allow Cl^- to serve as an internal tracer. The synthetic Sb(V) solutions had concentrations ranging from 2 to 15 mM, depending on the experiment, and were selected to correspond to 100 %, 200 %, or 500 % of the calculated reactive site capacity of the magnetite in each composite (i.e. 2, 4, and 10 mM in CS-rich aggregate experiments, and 3, 6, and 15 mM in CS-free aggregate experiments; Table 1). Calculations of Sb(V) concentrations were based on matching the total number of Sb molecules to a known percentage of the magnetite's surface reactive sites, allowing a fair comparison between the chitosan-containing and chitosan-free systems. The concentration of the reactive sites of magnetite in each pillar was estimated as:

$$[\text{–Fe–OH}]\ (\text{moles} \times \text{sites/L}) = Cs \times SSA \times d \times (10^{18}/N_A)$$ **(Equation (1)**,

where: Cs is the concentration of solid magnetite ($g{\cdot}L^{-1}$), SSA is the BET-determined specific surface area (70 $m^2{\cdot}g^{-1}$), d equals to 8 sites/nm^2, which is the theoretical crystallographic site density of magnetite (Wechsler et al., 1984), and N_A is the Avogadro constant.

The solutions were adjusted at a pH = 5.5, a value corresponding to a high adsorption capacity of Sb species (Leuz et al., 2006), and high enough to limit magnetite dissolution. Actually, the sorption capacity of Sb(V) has been reported to reach its maximum at acidic pH values, while it decreases at values higher than pH 6–8, on the contrary to Sb(III) whose sorption is pH independent (Filella and Williams, 2012). The dominant anionic species of dissolved Sb(V) at pH ≥ 3 is $Sb(OH)_6^-$, so its ability to be adsorbed electrostatically onto oxy(hydr)oxide minerals decreases beyond the point of zero charge of the binders (Filella and Williams, 2012). As such, experiments performed at pH values equal or higher than 6 were exempted from the current study. The same applied for highly acidic conditions, based on preliminary experiments that showed magnetite dissolution at least at pH up to 4. Concentrations of antimonate ($Sb(OH)_6^-$) and chloride (Cl^-) in the influent and effluent water were analyzed by a Dionex Integrion HPIC ion chromatography (Thermo scientific), to obtain break through curves.

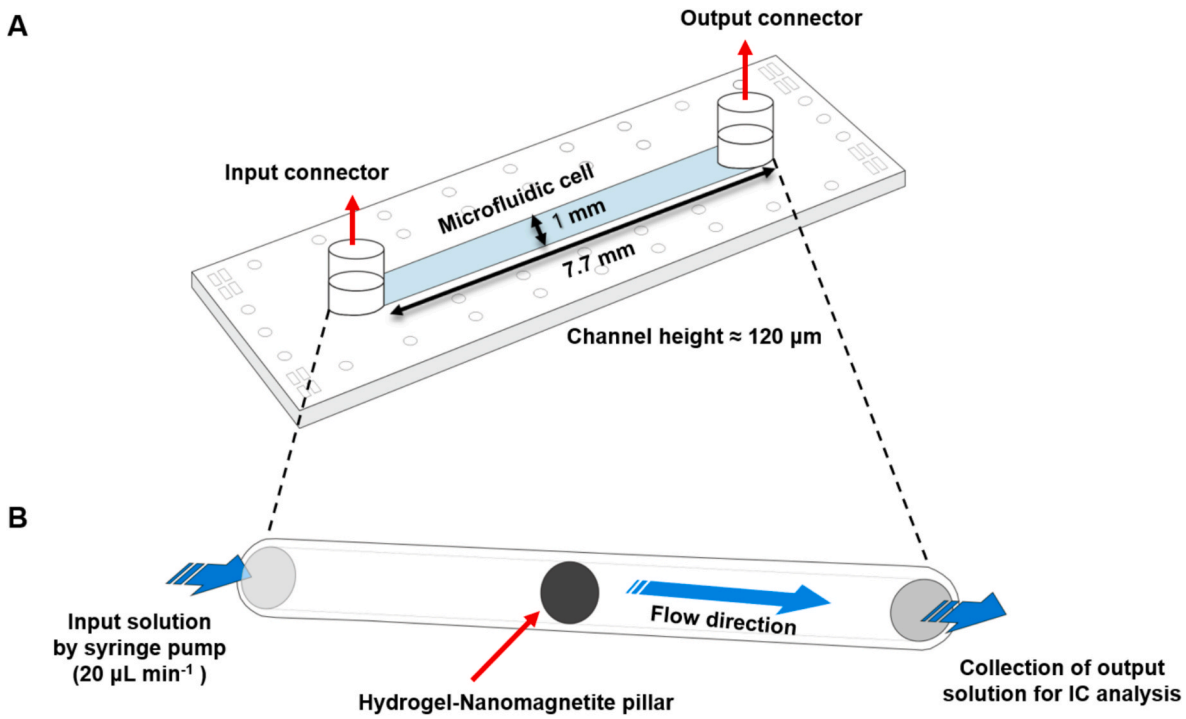

Fig. 1. Schematic depictions of **(A)** the microfluidic channel made of NOA (light blue) fixed on a glass slide, and **(B)** the experimental set-up, where Sb(V) solution flows through the channel and samples are regularly collected at the outlet for analysis.

Table 1
Description of the different flow-through experiments, including the details of the pillar composition, the concentration of magnetite nanoparticles in the respective hydrogel suspension that was used to form the pillars, the input Sb(V) concentration and its respective % reactive sites coverage of the magnetite nanoparticles present in the aggregate.

Sample	Hydrogel composition	[Nanomagnetite] g L^{-1}	$[Sb(V)]_{in}$ (mM)	% cover of NPs reactive sites
1a	PEGDA & Chitosan	2.318	2	100
1b	PEGDA & Chitosan	2.318	4	200
1c	PEGDA & Chitosan	2.318	10	500
2a	PEGDA	3.475	3	100
2b	PEGDA	3.475	6	200
2c	PEGDA	3.475	15	500

2.5. Synchrotron X-ray spectroscopy

Once each flow-through experiment was over (after around 24 h), transects of the cylinder sitting inside the microfluidic device were analyzed by μXAS. X-ray absorption near-edge structure (XANES) were collected at room temperature at the LUCIA beamline (Vantelon et al., 2016) at SOLEIL at the Sb L_3-edge (4.69 keV), a beamline which is sensitive to different Sb oxidation states (Rockenberger et al., 2000). Data were acquired with a beam size of 2.5 μm x 2.5 μm, in fluorescence mode, using a 60 mm^2 monoelement SDD detector (Bruker). At first, Sb mapping was performed by x-ray micro-fluorescence (μ-XRF) to map the diffusion of Sb within the cylindrical aggregates, and its relative abundance. Maps were acquired at 4400 eV in flyscan mode with a step size of 2 μm and 100 ms counting time. Then μXANES spectra were collected from the surface to the core-center of the cylinders, focusing on the interesting spots determined by the Sb mapping, to get Sb oxidation state data. PyMca software was used to process the μXRF data to deconvolute the XRF spectrum in each pixel of the maps, following Jupiter notebook application to correct the incident flux and the detector deadtime. Fiji software (ImageJ) was used for the illustration of the μXRF Sb concentration maps, and Athena software for the normalization of the μXAS data.

3. Results and discussion

3.1. Effluent solutions and break through curves

The effluent solution was collected regularly for $Sb(OH)_6^-$ and Cl^- measurement by Ion Chromatography. According to the results, a mean retardation time of about 200 min was estimated for Sb, and the system reached maximum efficiency for Sb removal after about 360 min (6 h) (Fig. 2). More specifically, during the first 260 min, a significant net removal of Sb was observed, indicating the effective adsorption of Sb onto the material. The system's performance can be understood in terms of a breakthrough curve (BTC), with an inflection point for chloride at around 10 min, which reflects the time it takes for chloride to start moving through the system, and a corresponding inflection for Sb at approximately 130 min, marking the point at which Sb begins to be effectively immobilized. The retardation factor, estimated at around 13, highlights the degree to which Sb is delayed in its migration through the system compared to chloride ions. This suggests that Sb is being efficiently adsorbed or retained by the material.

However, beyond the 360-minute mark, an increase in Sb concentration in the effluent—exceeding the initial input concentration—suggests that some of the sorbed Sb may be released back into the solution (Fig. 2). This could be due to desorption processes or the saturation of the adsorptive sites on the material, leading to the reversal of the adsorption process. Such behavior indicates that while the material is effective in removing Sb, there may be a limitation in terms of contaminant load or that desorption dynamics need to be further explored to fully understand the material's efficiency over extended periods. Additionally, a slight adsorption of chloride ions (Cl^-) is observed during the early stages of the experiment, followed by a phase

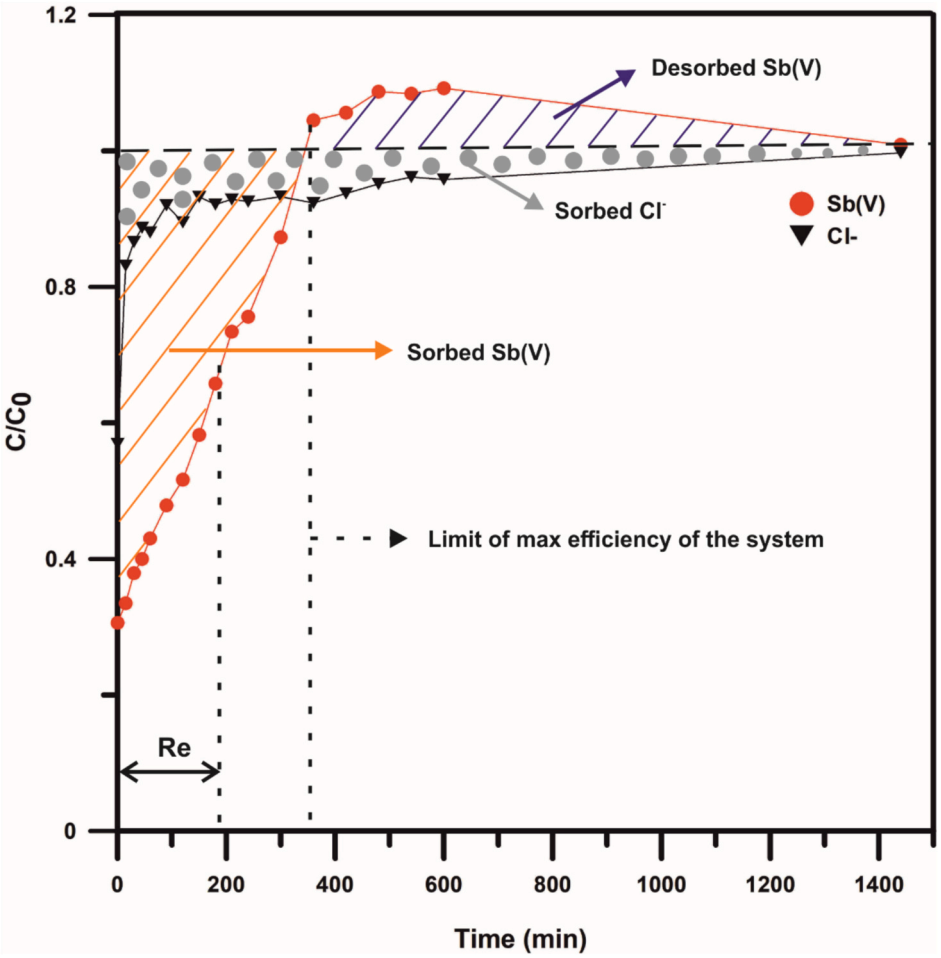

Fig. 2. Break-through curves of $Sb(OH)_6^-$ and Cl^- (tracer) effluent concentrations, showing the retardation time for Sb immobilization (first dashed line, Re) and its maximum removal efficiency throughout the microfluidic flow-through experiments (second dashed line). BTC correspond to selected experiment with conditions of pH 5.5, initial $[Sb(V)]_0 = 4$ mM, and in the presence of chitosan (sample 1b, Table 1).

of desorption **(**Fig. 2**)**. This phenomenon can be attributed to the small porosity of the samples, which initially limits the material's ability to fully expel chloride ions from the system. The adsorption of chloride is likely a result of the material's surface properties, where Cl^- ions might temporarily occupy available sites, but the desorption phase indicates that the material gradually releases Cl^- over time as equilibrium is approached. This behavior suggests that the material's porosity and surface characteristics play a significant role in the dynamic interactions

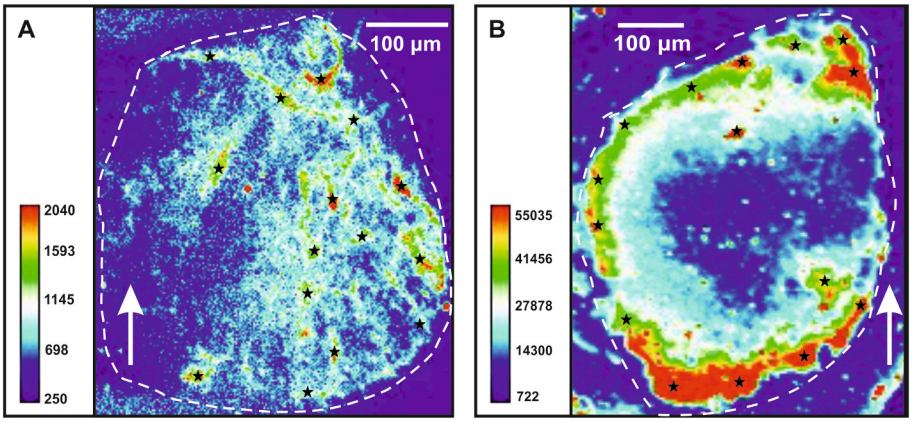

Fig. 3. Antimony (Sb) micro-x-ray fluorescence (µXRF) maps of the hydrogel-nanomagnetite composite pillar aggregates after 24 h of flow-through microfluidic experiments, illustrated by 'thermal' images created by Fiji software (ImageJ). The black stars correspond to the spots where the µXANES spectra were collected. Figure **(A)** corresponds to Sb(III) mapping in a PEGDA-nanomagnetite, chitosan-free, composite, with $[Sb(V)]_{in}$ being sufficient to cover 200% of the reactive sites of magnetite (sample 2b, Table 1). Figure **(B)** corresponds to Sb(V) mapping in chitosan-coated nanomagnetite-PEGDA composite, with $[Sb(V)]_{in}$ being sufficient to cover 500% of the reactive sites of magnetite (sample 1c, Table 1). Please note that different scale range on the color coding is given for the two images. The white arrows indicate the direction of the water flow through the microfluidic cells, and the dashed white outlines shape the pillars.

between the adsorbed species and the system.

3.2. Distribution of antimony within the aggregates

Antimony mapping by μ-XRF was performed for each polymer-nanomagnetite composite pillar while still sitting on the microfluidic cell after completion of the flow-through sorption experiments and the subsequent drying of the cells. The resulting images that show the relative abundance of $[Sb]_T$ though pillars subjected to 1-day flow-through sorption experiments are presented in Fig. 3. The sorbed Sb differs in concentration and distribution within the pillars depending on the initial concentration of Sb(V) ($[Sb(V)]_{in}$) in relation to the magnetite reactive site concentration in each aggregate, and the presence or absence of chitosan. When Sb(V) is injected at low initial concentrations, i.e. at 2 mM, or in chitosan-free aggregates, diffusion of antimony anions in the entire structure of the aggregate is observed **(**Fig. 3**A)**. This uniform distribution may indicate that at lower loading, the available reactive sites within the aggregate are not saturated, allowing Sb(V) to diffuse deeper before being adsorbed. It also reflects minimal electrostatic or steric hindrance within the matrix, possibly due to a more open internal pore network or the lack of interference from chitosan.

On the contrary, in the presence of chitosan, and/or at high $[Sb(V)]_{in}$, i.e., at 4 to 15 mM, Sb appears to be more efficiently immobilized, but to mostly accumulate at the edges of the pillars through surface adsorption **(**Fig. 3**B)**. This pattern suggests a diffusion-limited uptake mechanism, where high initial concentrations or modified surface interactions via chitosan lead to fast initial sorption near the inlet region, restricting further inward transport of Sb. The edges of the pillars, particularly near the fluid entry point, act as primary sorption zones. Antimonate ions enter the aggregate through its edge closer to the microfluidic cell input (lower central part of the aggregate, in Fig. 3), where they are mostly adsorbed. Important adsorption also, occurs at the exit of the aggregate closer to the fluid cell output (upper part of the aggregate, in Fig. 3**B**), mainly due the flow conditions in the wake of the hydrogel pillar. This accumulation suggests that the higher Sb concentrations or the presence of chitosan promote more localized interactions, with the edges of the pillars—potentially areas of higher surface area or reactivity—playing a critical role in Sb immobilization. Previous studies have shown that the content of magnetite nanoparticles in chitosan embedded composites might increase from the inner part to the surface of the aggregate depending on the synthesis procedure (Zou et al., 2011). Thus, the accumulation of Sb(V) mostly on the rim of the aggregates in presence of chitosan could be partly attributed to the uneven distribution of the magnetite nanoparticles in the pillars. These flow-dependent adsorption patterns highlight the importance of hydrodynamic conditions in defining sorption efficiency in flow-through systems.

Kinetics might also, play a role to the diffusion of Sb(V) within the aggregates, meaning that the duration of the current flow-through experiments might not allow for a more uniformly distribution throughout the pillars. The time-dependent distribution of arsenic (As) in chitosan-embedded Fe-oxides has been documented in prior studies (He et al., 2016), showing that a more uniform distribution of the sorbed species develops over time, such as after 72 h, which is three times longer than in the current experiments. This suggests that the operational time frame plays a critical role in achieving equilibrium distributions and optimizing overall material utilization.

The greater adsorption capacity of Sb onto chitosan rich composites is evident by the difference in the scale of the color coding corresponding to the x-ray fluorescence, which is 20–50 times higher **(**Fig. 3**B)** than in the case of the chitosan-free pillar **(**Fig. 3**A)**, and can be explained as follows. Chitosan was used originally to inhibit magnetite NP aggregation, but it also, happens to be a positively charged organic molecule at the pH of our experiments. Ferrous iron tends to be removed according to reaction **(1)**:

$$Fe_3O_4(s) + 2H^+ => Fe_2O_3(s) + Fe^{2+} + H_2O \quad (1)$$

Thus, an exchange for surface Fe(II) for chitosan positively charged molecule may occur, facilitating the binding of chitosan to the surface of the magnetite nanoparticles and, in turn, enabling it to bridge the mineral surface to the antimonite ions. Furthermore, in such a mechanism, chitosan may also inhibit Sb reduction by magnetite, by electrically isolating Sb from the mineral surface. Indeed, a reduction-free Sb adsorption is observed in the XANES spectra (described in detail in the following section), and this adsorption is higher in chitosan-coated magnetite **(**Fig. 4**B)** than in chitosan-free magnetite **(**Fig. 4**A)**. This suggests a dual role of the chitosan coating: (i) chitosan retains more efficiently the Fe oxide nanoparticles with Sb(V) bounding as ternary surface complex above an Fe(II) surface cavity (Kirsch et al., 2008), and/or (ii) Sb(V) bounds to the chitosan itself, after the latter (with two positive charges on the same molecule) replaces Fe(II) at the surface of magnetite. These findings confirm that chitosan modifies both the structural and electrochemical landscape of the composite, promoting stable Sb(V) adsorption via ternary surface complexation or direct binding.

Comparing the abundance of Sb in the studied pillars between the cases corresponding to Sb(III) **(**Fig. 3**A)** and Sb(V) **(**Fig. 3**B)** (identified by XANES), the lower sorption of Sb(III) could also, be explained by the low pH conditions. At pH values higher than the point of zero charge (PZC) (6–6.5), the magnetite surface becomes negatively charged, and by increasing the pH values it becomes more negative, facilitating the sorption of positively charged or neutral species via electrostatic attraction and specific inner-sphere complexation (Leng et al., 2012; Hassan et al., 2019). Thus, at the present pH conditions (5.5 < PZC) Sb (III) adsorption to magnetite is not highly favored, as antimonite ions primarily exist as the neutral species $Sb(OH)_3^0$. In contrast, Sb(V), which exists predominantly as the anionic species $Sb(OH)_6^-$ in solution, is strongly attracted to the positively charged magnetite surface at pH 5.5, making its adsorption more efficient and consistent with previous findings that favor anionic Sb(V) sorption onto Fe-oxy(hydr)oxide surfaces under acidic conditions (Filella and Williams, 2012). This behavior is consistent with previously reported As(V) and As(III) (behaving similarly to Sb species) adsorption via chitosan-Fe-oxide as the sorption agent (He et al., 2016). That study reports a faster adsorption of the pentavalent form of As compared to the trivalent one, a trend that may similarly apply to Sb, where Sb(V) is adsorbed more efficiently than Sb (III) under the given experimental conditions.

3.3. Sorbed antimony oxidation state

3.3.1. Reduction to Sb(III)

Antimony μ-XANES spectra were recorded at polymer-nanomagnetite pillar spots, characterized by high Sb accumulation, as identified via μXRF mapping **(**Fig. 3**)**. This targeted approach ensured that the measurements reflected areas of maximum sorption, providing insights into the redox behavior of antimony under varying conditions. Spectra obtained at $[Sb(V)]_{in}$ solution ranging from 2 to 6 mM are presented in Fig. 4**A**, and are compared to Sb(III) spectra. Spectra shape similarity points to Sb retention via reduction of Sb(V) to Sb(III) by magnetite when $[Sb(V)]_{in}$ was low (i.e., 3 to 6 mM) for chitosan-free magnetite —specifically when the input concentration does not exceed twice the estimated magnetite surface site concentration **(**Table 1**,** samples 2a and 2b**)**. Reduction to Sb(III) occurs, forming a stable, inner-sphere $FeOSb(OH)_2$ surface symmetrical sorption complex, in which Sb is at the position otherwise occupied by tetrahedral Fe(III) (Verbinnen et al., 2013; Kirsch et al., 2008). The reaction product diffuses throughout the entire aggregate structure, as expected from a neutral species ($Sb(OH)_3^0$) **(**Fig. 3**A)**. The resulted complexes are typically retained via strong sorption mechanisms that limit the mobility of Sb(III) in the environment. The stability of these sorbed species is enhanced by the redox-active surface of magnetite, which can further prevent

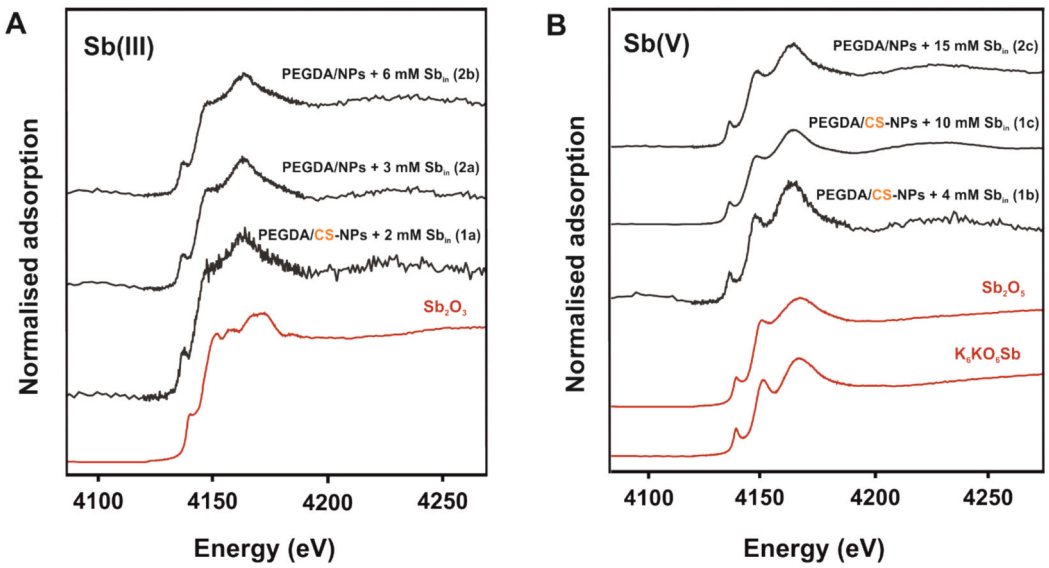

Fig. 4. Normalized XANES spectra, of references and samples after flow-through experiments run at different (i) Sb total input concentrations ($[Sb(V)]_{in}$), and/or (ii) hydrogel composition, at the Sb L_3 edge. **(A)** Sb(III) spectra ($[Sb(V)]_{in} \leq 6$ mM), and **(B)** Sb(V) spectra ($[Sb(V)]_{in} \geq 4$ mM). The name of each sample in parenthesis, for each spectrum, refers to Table 1. CS indicates the presence – if any – of chitosan as magnetite nanoparticle coating.

reoxidation and remobilization (Kirsch et al., 2008; Johnson et al., 2021). However, the degree of stability depends on environmental variables such as pH, competing ions, and the presence of oxidants (Zhang et al., 2022). Although sorption to magnetite can limit the immediate bioavailability and transport of Sb(III), experimental observations suggest that the stability of these sorbed species may vary under different environmental conditions, indicating they are not necessarily inert (Zhang et al., 2022; Johnson et al., 2021). Given that Sb speciation is influenced by redox-sensitive conditions and oxidative mineral surfaces, Sb(III) complexes may undergo reoxidation to Sb(V) in dynamic environments, potentially altering their mobility and environmental impact (Zhang et al., 2022). Overall, while Sb(III) complexes on magnetite are stable and reduce environmental risk under stable geochemical conditions, they may still pose a potential threat in dynamic or disturbed systems. These considerations underline the importance of accounting for site-specific conditions in predicting the long-term behavior of sorbed Sb species.

In presence of chitosan, the redox transformation of Sb(V) to Sb(III) becomes less pronounced. Reduction is only observed at the lowest tested Sb(V) input concentration (2 mM) **(**Fig. 4**A)**, which corresponds precisely to the magnetite surface site concentration (Table 1, sample 1a). This suggests that at low surface coverage, magnetite still facilitates redox conversion, but as Sb(V) concentration increases, the observed reduction effect becomes less prominent in the presence of chitosan. This trend does not necessarily indicate that chitosan chemically inhibits the redox reaction itself, but rather that it may influence the physical or spatial dynamics of the system. This is consistent with previous findings showing that pure chitosan does not alter the oxidation state of arsenic under O_2-free conditions (He et al., 2016), supporting the expectation of similar behavior for antimony due to their comparable redox properties. Therefore, while chitosan enhances the structural and functional integrity of the sorbent composite, its role in redox processes is more passive—modulating the microenvironment around magnetite rather than chemically dictating redox outcomes.

3.3.2. *Sb(V) surface adsorption*

Samples treated with higher $[Sb(V)]_{in}$ (from 4 to 15 mM) are compared to Sb(V) reference spectra and show an overall L_3 XANES edge dominated by Sb(V) **(**Fig. 4**B)**. This spectral similarity suggests that for chitosan-containing composites exposed to Sb(V) at initial concentrations corresponding to 200 % to 500 % coverage of the magnetite reactive sites **(**Table 1**,** samples 1b and 1c), reduction-free, surface adsorption is the driving Sb(V) immobilization mechanism. The enhanced immobilization of Sb(V) in these systems is evidenced by both μ-XRF mapping **(**Fig. 3**B)** and the respective XANES spectra **(**Fig. 4**B)**, which reveal substantial Sb accumulation in the outer regions of the composite pillars. This behavior suggests the occurrence of two distinct sorption pathways of Sb atoms. First, Sb(V) is likely retained via inner-sphere surface complexation with magnetite as $FeOSb(OH)_5^-$, a well-documented coordination mode for pentavalent antimony on iron oxide surfaces (Guo et al., 2014; Verbinnen et al., 2013; Kirsch et al., 2008). Second, a portion of antimonate ions may bond to the positively charged chitosan chains at the studied pH (~5.5), since NH_2 chitosan side chains become NH^{3+} at a pH environment less than their pKa (6.3) (Wang et al., 2006). As such, antimonate is most likely to be adsorbed as an outer-sphere complex, aligned with prior observations made for arsenate species interacting with chitosan-iron oxide systems (He et al., 2016).

In absence of chitosan, Sb(V) adsorption with no reduction is only observed at very high $[Sb(V)]_0$ input concentration (15 mM, enough to insure 500 % magnetite reactive surface site coverage) **(**Fig. 4**b;** Table 1**,** sample 2c**)**. This further highlights the role of chitosan in enhancing the sorption capacity of the composite by providing additional adsorption sites, rather than contributing directly to redox processes.

3.3.3. *Effect of pH and concentration to Sb sorption mechanisms*

It is important to consider the influence of pH on the redox behavior of Sb(V) in these systems. It has been shown that under anoxic conditions Sb(V) reduction is pH dependent and increases significantly at pH values larger than 6.5 (Verbinnen et al., 2013; Kirsch et al., 2008). Thus, since in the input solution pH is not higher than 5.5, these conditions might not allow maximum efficiency with respect to Sb(V) reduction to Sb(III). The limited Sb(V) reduction to its trivalent form by magnetite was also, reported by Kirsch et al. (2008), who showed hardly any reduction during similar experimental conditions (pH 5.0 to 6.0, around 22 hrs experiment). Poor reduction of As(V) by chitosan embedded Fe-oxide at similar pH conditions has been also, reported (He et al., 2016), corroborating the present Sb sorption processes, considering the similar geochemical behavior of the two redox sensitive species.

The contaminant load to the system appears to also, drive the sorption mechanisms of Sb to the presented system. At relatively high Sb concentrations enough to cover 200–500 % of magnetite reactive sites,

the surface redox reactions cannot function because the available surface sites on magnetite become saturated, leaving no additional reactive Fe-oxide sites to facilitate further electron transfer. Under these conditions, Sb(V) sticks on the outer layer of magnetite nanoparticles and is retained mostly by adsorption. In these scenarios, the sorbed Sb(III) concentration would be much lower than that of Sb(V) in our samples, so the overall signal-to-noise ratio becomes insufficient to conclusively identify Sb(III), and to confirm whether any partial reduction occurs under these conditions. Reduction beyond Sb(III) was not observed in any case, in agreement with other Sb sorption studies (Kirsch et al., 2008). The dependence of Sb(V) abiotic reduction on the concentration of Sb and the respective reactive sites of magnetite was pointed out by Zhang et al. (2022), who reported studies with distinct results on magnetite reactivity with respect to Sb reduction. For instance, limited Sb(V) reduction to Sb(III) by magnetite was observed at higher Sb(V) concentration, corresponding to higher Sb(V):magnetite ratio (Johnson et al., 2021), compared to lower Sb(V) concentration and Sb(V): magnetite ratio (Kirsch et al., 2008). This behavior is consistent with the efficient reduction of Sb(V) by magnetite observed at lower $[Sb(V)]_{in}$, and the limited reduction when the $[Sb(V)]_{in}$ surpasses the reactive surface sites of magnetite during our sorption experiments. These findings reinforce the conclusion that the abiotic reduction of Sb(V) by magnetite is strongly dependent on the balance between Sb concentration and the availability of reactive surface sites. When this balance is exceeded, sorption dominates over redox transformation, thereby limiting the extent of Sb(V) reduction under environmentally relevant conditions.

3.4. Comparison of hydrogel-nanomagnetite with other Sb sorbents

The Sb removal performance of the described system, along with key parameters from previous studies that used Fe-based materials for Sb immobilization, is summarized in Table 2. The comparison highlights differences in adsorption capacity, specific surface area (SSA), operational pH, and reaction conditions.

Zero-valent iron (ZVI) and its composites have been extensively studied due to their redox capability and strong affinity for Sb species. Unmodified ZVI demonstrates high capacity, though with notable drawbacks, as is prone to corrosion and has limited applicability in near-neutral pH environments (Dai et al., 2014). Among other ZVI composites, ZVI@CNT showed exceptionally high sorption capacity for both Sb (III) and Sb(V) at pH 5, but it requires strong acidic conditions, and suffers from particle aggregation and limited stability in long-term or flow-based systems (Mishra et al., 2016). Iron oxides like α-FeOOH and magnetite composites (e.g., Fe_3O_4@m-HNTs) offer improved environmental compatibility and work under a wider pH range (Zhu et al., 2017; Xiao et al., 2020). However, bare or weakly supported iron oxides often exhibit limited regeneration capability and poor mechanical stability in dynamic systems (Bai et al., 2022).

In contrast, the hydrogel-nanomagnetite composites presented in this study, while not expressed in mg/g due to their composite nature, show a high surface-specific Sb sorption efficiency (8 atoms/nm^2)—outperforming many conventional sorbents such as ZVI@PVA (Zhao et al., 2014), Fe_3O_4@m-HNTs (Zhu et al., 2017), and a-FeOOH (Xiao et al., 2020). Notably, the current system operates efficiently under flow-through microfluidic conditions, a significant practical advantage over batch-based systems reported in the literature. Moreover, chitosan-coated composites enhance Sb(V) retention through electrostatic attraction, while chitosan-free composites support reduction of Sb(V) to Sb(III) in addition to surface adsorption, depending on the concentration input. This dual mechanism of adsorption and redox transformation is rarely found in a single material. The hydrogel matrix prevents nanoparticle aggregation, supports magnetic recovery, and facilitates filtration process—features not often co-optimized in high-capacity sorbents such as ZVI@CNT (Mishra et al., 2016) or Fe-Zr composites (Li et al., 2012). Although the total mass-based adsorption capacity of the current composite system does not always surpass other sorbents, its unique combination of high surface efficiency, flow compatibility, and material stability, makes it a compelling candidate for future water treatment technologies.

Overall, this study distinguishes itself by coupling redox-active nanomagnetite with hydrogel-based structural support, integrating the system into a flow-through microfluidic platform. This approach enables not only efficient Sb removal through both adsorption and redox mechanisms, but also direct spatial and speciation analysis via synchrotron μ-XRF/μ-XANES. To our knowledge, this is the first report of a structurally stable, magnetically recoverable, and redox-active composite evaluated under microfluidic flow for Sb immobilization. These aspects mark a significant advancement over existing batch-based systems and demonstrate clear potential for real-world, scalable water treatment applications.

4. Environmental relevance

This work provides insights into the role of Fe II/III oxides into the immobilization of Sb, offering a novel remediation strategy for both drinking and wastewater—particularly in aquatic systems impacted by prolonged exposure to industrial and mining activities. A notable example includes the world's largest Sb mining area of Xikuangshan, China (Fu et al., 2023). Another application scenario might be the remediation of rivers and estuarine systems affected by long-term exposure to mining activities resulting in AMD-contaminated environments, such as the Tinto and Odiel Estuaries (SW Spain) that contribute significantly to the total contamination of the Atlantic Ocean (Braungardt et al., 2003; Nieto et al., 2013).

A key advantage of the present study is the use of materials that

Table 2
Comparison of Sb(V) removal performance by various iron-based materials, including relevant operational and material parameters. The table is modified after Bai et al. (2022). The sorption capacity expressed in atoms Sb/nm^2 (equal to d − surface site density of the material) for the different studies was calculated according to Equation (1), considering the input Sb(V) concentration as the concentration of the reactive sites of each adsorbent.

Adsorbent	Sorption capacity (mg/g)	SSA (m^2/g)	Sorption capacity (atoms Sb/nm^2)	pH	Input concentration (mg/L)	Reaction time (h)	References
ZVI	55.56	–	–	4	20–260	3	(Dai et al., 2014)
ZVI@PVA	1.65	11.3	1.1	7	5	48	(Zhao et al., 2014)
ZVI@CNT	250	132	0.8	5	50	4	(Mishra et al., 2016)
Fe_3O_4@m-HNTs	30.49	23.791	4.2	5	20	12	(Zhu et al., 2017)
C8-Fe_3O_4@SiO_2	3.5	–	–	5	0.2	4	(Li et al., 2015)
a-FeOOH	102.67	186.25	0.5	7	10	0.8	(Xiao et al., 2020)
Fe-Zr	51	121	–	7	0–25	24	(Li et al., 2012)
Ce-Fe_3O_4	188.1	152.2	8.1	7	50	12	(Qi et al., 2017)
Zn-Fe@LDH	122.03	11.9	3.2	7	2	24	(Lu et al., 2015)
PEGDA/CS-Fe_3O_4	–	70	8	5.5	206	6	Present study

combine the great contaminants' adsorption capacity of magnetite nanoparticles with the beneficial properties of polymeric coatings (i.e., PEGDA and chitosan), which may facilitate the remediation process. Magnetic iron oxides such as Fe_3O_4 are considerably advantageous given their simple and low-cost preparation, and their low toxicity (Hassan et al., 2019). However, pure nanoparticles pose practical challenges in flow-through systems, where high head loss in fixed-column treatment units limits their application (Sarkar et al., 2012). In contrast, the bio-nanocomposites developed in this study—owing to their increased size, mechanical durability, and non-swelling behavior—are better suited for use in real hydraulic systems. These composites simplify downstream filtration and separation, while offering sustained sorption capacity and reusability (He et al., 2016; Long et al., 2020). More specifically, the hydrogel-nanomagnetite composite demonstrates promising characteristics for sustainable water treatment applications, particularly in terms of long-term operational stability, regeneration efficiency, and reuse performance. Its structural integrity helps prevent nanoparticle aggregation, while maintaining porosity and swelling behavior, both essential for effective and prolonged contaminant uptake. Reusability across multiple treatment cycles further enhances its suitability for cost-effective, large-scale deployment.

Nonetheless, to scale up for real-field applications, future studies must address several key aspects. Sorption experiments should be conducted under more acidic pH levels (4–5) to enhance Sb(V) adsorption, as well as under alkaline pH conditions (7–8) to favor the reduction to Sb (III) (Kirsch et al., 2008), although this should limit Sb immobilization by surface adsorption. Optimization of both the microfluidic system and the composite matrix of the hydrogel-nanomagnetite aggregates will be critical for developing a competitive and efficient Sb sorbent material, which can outperform existing alternatives. These experiments will be essential to refine the material's performance, ensuring its applicability in real-world scenarios where complex environmental factors, such as ionic strength and competing contaminants, are present.

Finally, while this method is developed with Sb in mind, the platform shows potential for remediating a broader range of redox-sensitive inorganic contaminants—such as arsenic (As), chromium (Cr), uranium (U), and molybdenum (Mo). Future studies targeting these elements will be critical for broadening the material's applicability and maximizing its environmental impact.

5. Conclusions

Leveraging the well-established capacity of pure magnetite to adsorb and reduce Sb, this study investigates bio-nanocomposites and the influence of polymeric coatings on redox interactions between magnetite and Sb species. For the first time, microfluidic technology is integrated with controlled kinetic experiments and μXAS analysis to investigate the mobility and retention mechanisms of Sb within nanomagnetite aggregates.

The hydrogel-nanomagnetite composites examined here offer a stable and regenerative platform for water purification processes, combining the biocompatibility and functional versatility of natural polymers with the magnetic responsiveness and high surface area of nanomaterials. Compared to conventional Sb adsorbents such as zero-valent iron and bulk iron oxides, these composites offer a distinctive balance of performance, cost-effectiveness, and operational ease. Unlike many traditional materials that either lack magnetic recovery or require post-treatment stabilization, these composites inherently support easy separation, sustained reactivity, and long-term mechanical integrity—making them particularly well-suited for continuous flow-through systems.

A key contribution of this work is the detailed understanding of Sb redox behavior, highlighting how immobilization mechanisms are influenced by the concentration of Sb(V) and the presence of chitosan. Specifically, when Sb(V) levels are low—up to twice the number of reactive sites on magnetite nanoparticles—and chitosan is absent, reductive precipitation to Sb(III) is the dominant retention pathway. In contrast, at higher Sb(V) concentrations, particularly in systems incorporating chitosan-coated nanoparticles, surface adsorption becomes the primary mechanism, accompanied by limited reduction, while leading to enhanced Sb retention. These findings confirm that polymeric coatings not only modulate the redox environment but also boost Sb retention efficiency by magnetite, thus supporting their promise for water treatment applications.

Despite ongoing advances in antimony speciation and remediation research, studies that directly examine redox kinetics and contaminant mobility in magnetite-based systems—particularly under dynamic flow conditions—remain scarce. By integrating microfluidic experimentation with high-resolution X-ray spectroscopy, this study offers a novel and transferable platform for evaluating such processes under controlled conditions. The insights gained here lay essential groundwork for a scalable Sb treatment approach, highlighting the potential of nanocomposite materials for real-world deployment in mining, industrial, and rural water systems, where resilience, safety, and cost-efficiency are critical. More broadly, these findings contribute to the global advancement of sustainable technologies aimed at mitigating redox-sensitive contaminants in both drinking and wastewater environments.

Funding Sources

This work was supported by the European Union's Horizon 2020 research and innovation programme under the Marie Skłodowska-Curie grant agreement No. 892,570 (REPONANO project). Dr. Hervé Tabuteau was supported by the ANR INFLOW (ANR-21-CE29-0008).

CRediT authorship contribution statement

Evgenia-Maria Papaslioti: Writing – original draft, Visualization, Validation, Project administration, Methodology, Investigation, Funding acquisition, Formal analysis, Data curation, Conceptualization. **Hervé Tabuteau:** Writing – review & editing, Visualization, Methodology, Formal analysis, Data curation. **Julien Farasin:** Visualization, Methodology, Data curation. **Delphine Vantelon:** Writing – review & editing, Visualization, Methodology, Formal analysis, Data curation. **Valerie Magnin:** Methodology, Data curation. **Laurent Charlet:** Writing – review & editing, Validation, Supervision, Project administration, Investigation, Funding acquisition, Conceptualization.

Declaration of competing interest

The authors declare that they have no known competing financial interests or personal relationships that could have appeared to influence the work reported in this paper.

Acknowledgments

Dr. Evgenia-Maria Papaslioti acknowledges the financial support by the European Union's Horizon 2020 research and innovation program under the Marie Skłodowska-Curie grant agreement No. 892570. Dr. Hervé Tabuteau was supported by the ANR INFLOW (ANR-21-CE29-0008). We are grateful to Dr. Delphine Tisserand and Dr. Simona Denti for their assistance during laboratory and analytical work, and to Carolina Guida for her valuable help during the microfluidic experiments. Experiments and analyses were performed within the analytical chemistry platform of ISTerre (OSUG France). We acknowledge SOLEIL for provision of synchrotron radiation facilities and we would like to thank the staff for assistance in using beamline "LUCIA" and especially, Dr. Camille Rivard for her technical support in the μXRF maps interpretation.

Data availability

Data will be made available on request.

References

Filella, M., Belzile, N., Chen, Y.W., 2002. Antimony in the environment: a review focused on natural waters: I. Occurrence. Earth Sci. Rev. 57 (1–2), 125–176. https://doi.org/10.1016/S0012-8252(01)00070-8.

United States Environmental Protection Agency, 1979. Water Related Fate of the 129 Priority Pollutants, vol. 1. USEPA, Washington, DC, USA, EP-440r4-79-029A.

Council of the European Communities, 1976. Council Directive 76r464rEEC of 4 May 1976 on pollution caused by certain dangerous substances discharged into the aquatic environment of the Community. Official Journal L 129, 18r05r1976, pp. 23–29.

Council of the European Union, 1998. Council Directive 98/83/EC of 3 November 1998 on the quality of water intended for human consumption. Official Journal L 330, 05/12/1998, pp. 32–54.

Wilson, S.C., Lockwood, P.V., Ashley, P.M., Tighe, M., 2010. The chemistry and behaviour of antimony in the soil environment with comparisons to arsenic: a critical review. Environ. Pollut. 158 (5), 1169–1181. https://doi.org/10.1016/j.envpol.2009.10.045.

Boreiko, C.J., Rossman, T.G., 2020. Antimony and its compounds: Health impacts related to pulmonary toxicity, cancer, and genotoxicity. Toxicol. Appl. Pharmacol. 403, 115156. https://doi.org/10.1016/j.taap.2020.115156.

Fu, X., Xie, X., Charlet, L., He, J., 2023. A review on distribution, biogeochemistry of antimony in water and its environmental risk. J. Hydrol. 130043. https://doi.org/10.1016/j.jhydrol.2023.130043.

Zhang, Y., O'Loughlin, E.J., Kwon, M.J., 2022. Antimony redox processes in the environment: a critical review of associated oxidants and reductants. J. Hazard. Mater. 431, 128607. https://doi.org/10.1016/j.jhazmat.2022.128607.

Filella, M., Williams, P.A., Belzile, N., 2009. Antimony in the environment: knowns and unknowns. Environ. Chem. 6 (2), 95–105. https://doi.org/10.1071/EN09007.

Guo, X., Wu, Z., He, M., Meng, X., Jin, X., Qiu, N., Zhang, J., 2014. Adsorption of antimony onto iron oxyhydroxides: adsorption behavior and surface structure. J. Hazard. Mater. 276, 339–345. https://doi.org/10.1016/j.jhazmat.2014.05.025.

Qi, P., Pichler, T., 2016. Sequential and simultaneous adsorption of Sb (III) and Sb (V) on ferrihydrite: Implications for oxidation and competition. Chemosphere 145, 55–60. https://doi.org/10.1016/j.chemosphere.2015.11.057.

Casiot, C., Ujevic, M., Munoz, M., Seidel, J.L., Elbaz-Poulichet, F., 2007. Antimony and arsenic mobility in a creek draining an antimony mine abandoned 85 years ago (upper Orb basin, France). Appl. Geochem. 22 (4), 788–798. https://doi.org/10.1016/j.apgeochem.2006.11.007.

Missana, T., Alonso, U., Scheinost, A.C., Granizo, N., García-Gutiérrez, M., 2009. Selenite retention by nanocrystalline magnetite: Role of adsorption, reduction and dissolution/co-precipitation processes. Geochim. Cosmochim. Acta 73 (20), 6205–6217. https://doi.org/10.1016/j.gca.2009.07.005.

Verbinnen, B., Block, C., Lievens, P., Van Brecht, A., Vandecasteele, C., 2013. Simultaneous removal of molybdenum, antimony and selenium oxyanions from wastewater by adsorption on supported magnetite. Waste Biomass Valoriz. 4, 635–645. https://doi.org/10.1007/s12649-013-9200-8.

Pallud, C., Masue-Slowey, Y., Fendorf, S., 2010. Aggregate-scale spatial heterogeneity in reductive transformation of ferrihydrite resulting from coupled biogeochemical and physical processes. Geochim. Cosmochim. Acta 74 (10), 2811–2825. https://doi.org/10.1016/j.gca.2010.01.032.

Kirsch, R., Scheinost, A.C., Rossberg, A., Banerjee, D., Charlet, L., 2008. Reduction of antimony by nano-particulate magnetite and mackinawite. Mineral. Mag. 72 (1), 185–189. https://doi.org/10.1180/minmag.2008.072.1.185.

Mittal, V.K., Bera, S., Narasimhan, S.V., Velmurugan, S., 2013. Adsorption behavior of antimony (III) oxyanions on magnetite surface in aqueous organic acid environment. Appl. Surf. Sci. 266, 272–279. https://doi.org/10.1016/j.apsusc.2012.12.010.

Wu, W., He, Q., Jiang, C., 2008. Magnetic iron oxide nanoparticles: synthesis and surface functionalization strategies. Nanoscale Res. Lett. 3, 397–415. https://doi.org/10.1007/s11671-008-9174-9.

He, J., Bardelli, F., Gehin, A., Silvester, E., Charlet, L., 2016. Novel chitosan goethite bionanocomposite beads for arsenic remediation. Water Res. 101, 1–9. https://doi.org/10.1016/j.watres.2016.05.032.

Wang, Y., Li, B., Zhou, Y., Jia, D., 2009. In situ mineralization of magnetite nanoparticles in chitosan hydrogel. Nanoscale Res. Lett. 4 (9), 1041–1046. https://doi.org/10.1007/s11671-009-9355-1.

Zou, W., Geng, H., Lin, M., Xiong, X., 2011. Facile one-pot preparation of superparamagnetic chitosan sphere and its derived hollow sphere. J. Appl. Polym. Sci. 123 (6), 3587–3594. https://doi.org/10.1002/app.34887.

Maher, K., Mayer, K.U., 2019. Tracking diverse minerals, hungry organisms, and dangerous contaminants using reactive transport models. Elements: an International Magazine of Mineralogy, Geochemistry, and Petrology 15 (2), 81–86. https://doi.org/10.2138/gselements.15.2.81.

Wielinski, J., Jimenez-Martinez, J., Göttlicher, J., Steininger, R., Mangold, S., Hug, S.J., Voegelin, A., 2022. Spatiotemporal mineral phase evolution and arsenic retention in microfluidic models of zerovalent iron-based water treatment. Environ. Sci. Tech. 56 (19), 13696–13708. https://doi.org/10.1021/acs.est.2c02189.

Mubarak, H., Chai, L.Y., Mirza, N., Yang, Z.H., Pervez, A., Tariq, M., Mahmood, Q., 2015. Antimony (Sb)–pollution and removal techniques–critical assessment of technologies. Toxicol. Environ. Chem. 97 (10), 1296–1318. https://doi.org/10.1080/02772248.2015.1095549.

Long, X., Wang, X., Guo, X., He, M., 2020. A review of removal technology for antimony in aqueous solution. J. Environ. Sci. 90, 189–204. https://doi.org/10.1016/j.jes.2019.12.008.

Bai, Y., Tang, X., Sun, L., Yin, W., Hu, G., Liu, M., Gong, Y., 2022. Application of iron-based materials for removal of antimony and arsenic from water: Sorption properties and mechanism insights. Chem. Eng. J. 431, 134143. https://doi.org/10.1016/j.cej.2021.134143.

Jolivet, J.P., Belleville, P., Tronc, E., Livage, J., 1992. Influence of Fe (II) on the formation of the spinel iron oxide in alkaline medium. Clay Clay Miner. 40, 531–539. https://doi.org/10.1346/CCMN.1992.0400506.

Poulain, A., Fernandez-Martinez, A., Greneche, J.M., Prieur, D., Scheinost, A.C., Menguy, N., Charlet, L., 2022. Selenium nanowire formation by reacting selenate with magnetite. Environ. Sci. Tech. 56 (20), 14817–14827. https://doi.org/10.1021/acs.est.1c08377.

de Alvarenga, E.S., 2011. Characterization and properties of chitosan. Biotechnology of Biopolymers 91, 48–53.

Milonjić, S., Kopečni, M., Ilić, Z., 1983. The point of zero charge and adsorption properties of natural magnetite. J. Radioanal. Nucl. Chem. 78 (1), 15–24. https://doi.org/10.1007/bf02519745.

Kosmulski, M., 2004. pH-dependent surface charging and points of zero charge II. Update. J. Colloid Interface Sci. 275 (1), 214–224. https://doi.org/10.1016/j.jcis.2006.01.003.

Weinhausen, B., Köster, S., 2013. Microfluidic devices for X-ray studies on hydrated cells. Lab Chip 13 (2), 212–215. https://doi.org/10.1039/C2LC41014A.

Neckel, I.T., de Castro, L.F., Callefo, F., Teixeira, V.C., Gobbi, A.L., Piazzetta, M.H., Tolentino, H.C., 2021. Development of a sticker sealed microfluidic device for in situ analytical measurements using synchrotron radiation. Sci. Rep. 11 (1), 23671. https://doi.org/10.1038/s41598-021-02928-2.

Wechsler, B.A., Lindsley, D.H., Prewitt, C.T., 1984. Crystal structure and cation distribution in titanomagnetites (Fe3-xTixO4). Am. Mineral. 69 (7–8), 754–770.

Leuz, A.K., Mönch, H., Johnson, C.A., 2006. Sorption of Sb (III) and Sb (V) to goethite: influence on Sb (III) oxidation and mobilization. Environ. Sci. Tech. 40 (23), 7277–7282. https://doi.org/10.1021/es061284b.

Filella, M., Williams, P.A., 2012. Antimony interactions with heterogeneous complexants in waters, sediments and soils: a review of binding data for homologous compounds. Geochemistry 72, 49–65. https://doi.org/10.1016/j.chemer.2012.01.006.

Vantelon, D., Trcera, N., Roy, D., Moreno, T., Mailly, D., Guilet, S., Delmotte, F., Meltchakov, E., Lassalle, B., Lagarde, P., Flank, A.-M., 2016. The LUCIA beamline at SOLEIL. J. Synchrotron Radiat. 23 (2), 635–640.

Rockenberger, J., Zum Felde, U., Tischer, M., Tröger, L., Haase, M., Weller, H., 2000. Near edge X-ray absorption fine structure measurements (XANES) and extended X-ray absorption fine structure measurements (EXAFS) of the valence state and coordination of antimony in doped nanocrystalline SnO 2. J. Chem. Phys. 112 (9), 4296–4304. https://doi.org/10.1063/1.480975.

Leng, Y., Guo, W., Su, S., Yi, C., Xing, L., 2012. Removal of antimony (III) from aqueous solution by graphene as an adsorbent. Chem. Eng. J. 211, 406–411. https://doi.org/10.1016/j.cej.2012.09.078.

Hassan, A., Sorour, N.M., El-Baz, A., Shetaia, Y., 2019. Simple synthesis of bacterial cellulose/magnetite nanoparticles composite for the removal of antimony from aqueous solution. Int. J. Environ. Sci. Technol. 16, 1433–1448.

Johnson, C.R., Antonopoulos, D.A., Boyanov, M.I., Flynn, T.M., Koval, J.C., Kemner, K.M., O'Loughlin, E.J., 2021. Reduction of Sb (V) by coupled biotic-abiotic processes under sulfidogenic conditions. Heliyon 7 (2).

Wang, Q.Z., Chen, X.G., Liu, N., Wang, S.X., Liu, C.S., Meng, X.H., Liu, C.G., 2006. Protonation constants of chitosan with different molecular weight and degree of deacetylation. Carbohydr. Polym. 65 (2), 194–201. https://doi.org/10.1016/j.carbpol.2006.01.001.

Dai, C., Zhou, Z., Zhou, X., Zhang, Y., 2014. Removal of Sb (III) and Sb (V) from aqueous solutions using nZVI. Water Air Soil Pollut. 225, 1–12. https://doi.org/10.1007/s11270-013-1799-3.

Zhao, X., Dou, X., Mohan, D., Pittman Jr, C.U., Ok, Y.S., Jin, X., 2014. Antimonate and antimonite adsorption by a polyvinyl alcohol-stabilized granular adsorbent containing nanoscale zero-valent iron. Chem. Eng. J. 247, 250–257. https://doi.org/10.1016/j.cej.2014.02.096.

Mishra, S., Dwivedi, J., Kumar, A., Sankararamakrishnan, N., 2016. Removal of antimonite (Sb (III)) and antimonate (Sb (V)) using zerovalent iron decorated functionalized carbon nanotubes. RSC Adv. 6 (98), 95865–95878. https://doi.org/10.1039/C6RA18965B.

Zhu, K., Duan, Y., Wang, F., Gao, P., Jia, H., Ma, C., Wang, C., 2017. Silane-modified halloysite/Fe3O4 nanocomposites: Simultaneous removal of Cr (VI) and Sb (V) and positive effects of Cr (VI) on Sb (V) adsorption. Chem. Eng. J. 311, 236–246. https://doi.org/10.1016/j.cej.2016.11.101.

Li, P., Chen, Y.J., Hu, X., Lian, H.Z., 2015. Magnetic solid phase extraction for the determination of trace antimony species in water by inductively coupled plasma mass spectrometry. Talanta 134, 292–297. https://doi.org/10.1016/j.talanta.2014.11.026.

Xiao, M., Zhao, Y., Li, S., 2020. Facile synthesis of chrysanthemum-like mesoporous α-FeOOH and its adsorptive behavior of antimony from aqueous solution. J. Dispers. Sci. Technol. 41 (12), 1812–1820. https://doi.org/10.1080/01932691.2019.1637263.

Li, X., Dou, X., Li, J., 2012. Antimony (V) removal from water by iron-zirconium bimetal oxide: Performance and mechanism. J. Environ. Sci. 24 (7), 1197–1203. https://doi.org/10.1016/S1001-0742(11)60932-7.

Qi, Z., Joshi, T.P., Liu, R., Liu, H., Qu, J., 2017. Synthesis of Ce (III)-doped Fe3O4 magnetic particles for efficient removal of antimony from aqueous solution. J. Hazard. Mater. 329, 193–204. https://doi.org/10.1016/j.jhazmat.2017.01.007.

Lu, H., Zhu, Z., Zhang, H., Zhu, J., Qiu, Y., 2015. Simultaneous removal of arsenate and antimonate in simulated and practical water samples by adsorption onto Zn/Fe layered double hydroxide. Chem. Eng. J. 276, 365–375. https://doi.org/10.1016/j.cej.2015.04.095.

Braungardt, C.B., Achterberg, E.P., Elbaz-Poulichet, F., Morley, N.H., 2003. Metal geochemistry in a mine-polluted estuarine system in Spain. Appl. Geochem. 18 (11), 1757–1771. https://doi.org/10.1016/S0883-2927(03)00079-9.

Nieto, J.M., Sarmiento, A.M., Canovas, C.R., Olias, M., Ayora, C., 2013. Acid mine drainage in the Iberian Pyrite Belt: 1. Hydrochemical characteristics and pollutant load of the Tinto and Odiel rivers. Environ. Sci. Pollut. Res. 20, 7509–7519. https://doi.org/10.1007/s11356-013-1634-9.

Sarkar, S., Guibal, E., Quignard, F., SenGupta, A.K., 2012. Polymer-supported metals and metal oxide nanoparticles: synthesis, characterization, and applications. J. Nanopart. Res. 14, 1–24. https://doi.org/10.1007/s11051-011-0715-2.